Figures of merit and optimization of a VO_2 microbolometer with strong electrothermal feedback

Gilson Neto
L. Alberto L. de Almeida
Universidade Federal da Bahia
Department of Electrical Engineering
Salvador—BA, Brazil

Antonio M. N. Lima
Cleumar S. Moreira
Helmut Neff
Universidade Federal de Campina Grande
Center for Electrical Engineering and Informatics
Department of Electrical Engineering
58109-000 Campina Grande—PB, Brazil
E-mail: amnlima@dee.ufcg.edu.br

Igor A. Khrebtov
Valery G. Malyarov
State Scientific Center of the Russian Federation
Vavilov Optical Institute
St. Petersburg, Russia

Abstract. The influence of electrothermal feedback and hysteresis on the operation conditions, noise, and performance of a VO_2 transition-edge microbolometer has been evaluated. The material undergoes a first-order semiconductor-to-metal phase transition (SMT) within the temperature range $40 < T < 70\ °C$. Due to electrothermal feedback, all device parameters, including the required heat-sink temperature, output voltage and current response, response time, linear dynamic range, responsivity, noise, and detectivity, display complex and nonlinear variations with temperature, electrical biasing conditions, input radiation levels, and hysteresis width. In the constant-current mode, the device responsivity extends over a broad temperature range, but under constant-voltage operation it is sharply localized and restricted to the SMT center. Film quality, as represented by the transition and the hysteresis width and the flicker noise magnitude, crucially affects device performance. In the weak hysteretic case and at low $1/f$ noise levels, the device detectivity improves substantially in both operation modes. The spectral range of the device is largely determined by the optical absorptivity of the VO_2 film. For operation within the SMT, it extends well into the far IR wavelength region of the atmospheric window, but is substantially smaller for operation in the semiconducting region. [DOI: 10.1117/1.2956386]

Subject terms: thermal sensor; modeling; semiconductor-metal transition; metal-insulator transition; transition edge; microbolometer; vanadium dioxide; electrothermal feedback; hysteresis.

Paper 070874RR received Oct. 28, 2007; revised manuscript received May 3, 2008; accepted for publication May 11, 2008; published online Jul. 29, 2008.

1 Introduction

Uncooled infrared imaging systems are lightweight, demand low power, and are much less expensive than cooled infrared quantum detectors. However, most present devices operate in the semiconducting phase and thus exhibit low detectivity ($D^* < 10^7$ cm Hz$^{1/2}$ W^{-1}). Moving the operating point of these devices toward the transition region may increase the detectivity by several orders of magnitude. However, when operated in this region these devices usually exhibit hysteresis, a largely disregarded complex, nonlinear, and history-dependent phenomenon. So far, evaluation of the expected performance of a vanadium dioxide (VO_2) transition edge device has not been possible because of the lack of a suited theoretical model. Quite recently, researchers at North Carolina State University have succeeded in making very high-quality VO_2 films, almost hysteresis-free, which should allow high detectivity ($D^* > 10^8$ cm Hz$^{1/2}$ W^{-1}).

Transition-edge microbolometers have attracted renewed attention as sensitive, spectrally broadband radiation-sensing devices. Applications also include fast-responding microcalorimeters for x-ray, γ-ray, and nuclear particle detection, and bolometer mixers.[2] The physical function and optimization of superconducting low- and high-T_C transition-edge devices are now well understood. Instruments showing superior performance have been realized.[3,4] However, design and operation of superconducting transition-edge devices is technically demanding and expensive, due to the need for cooling and control at cryogenic temperatures. Recently, nonstoichiometric vanadium dioxide and tungsten-doped array configurations, exhibiting improved operation at ambient temperature, have been exploited in the absence of a phase transition, using advanced micromachining technology.[5,6]

Here, we extend the hysteresis model proposed in Ref. 7 to evaluate the bolometric figures of merit and performance of VO_2-based transition edge sensors. VO_2-based radiometric sensors can be operated in both the anhysteretic, semiconducting state at lower T and as transition-edge devices within a very fast-switching semiconductor-to-metal solid-state phase transition. The electronic solid-state transition appears slightly above ambient temperature, which substantially simplifies the use of the instrument. Devices can be operated under electrical current or voltage biases (I_b or V_b) while maintaining strong electrothermal feedback (ETF) conditions. ETF in transition-edge devices leads to pronounced nonlinear behavior. Such effects are mainly caused by temperature- and bias-dependent Joule heating or cool-

0091-3286/2008/$25.00 © 2008 SPIE

ing $dJ_{V,I}$ of the sensing element, and linked to strong temperature-induced film resistance variations dR_S. Quantitatively, ETF is described by the variation of $dJ_{V,I}/dR_S$. Thus, for materials that exhibit negative values of the temperature coefficient of resistance (TCR) β, operation in the constant-current mode (CCM) causes a decrease ($dJ_I = -I^2 \beta R_S\, dT$) on radiation heating dT, and the electrothermal feedback is negative. In contrast the constant-voltage mode (CVM), exhibiting positive ETF, leads to an increase in dJ ($dJ_V = +V^2 \beta\, dT/R_S$).

For polycrystalline and epitaxial VO_2 films, as well as bulk crystals, the semiconductor-to-metal phase transition (SMT) is well established over an extended period[8,9] covering a transition temperature range 40 to 70 °C. The physical mechanism and origin of the SMT in VO_2 still appear controversial, but are linked to a delicate, temperature-affected interplay and balance between the electron-electron correlations of a Mott-Hubbard insulator and an ordinary metal.[1] A further yet little explored and interesting feature is the presence of a pronounced negative differential resistance effect in the current-voltage characteristics, induced within the transition region by Joule self-heating.[10] All attempts at accurate modeling and optimization of VO_2-based microbolometers for improving the achievable figures of merit in device operation are severely hampered by the hysteretic nature of the phase-transition. Phase switching properties of VO_2-V_2O_5 films and applications to optical switches and bolometric light detectors have been reported in Refs. 11 and 12.

Analysis of the thermal-device–radiation interaction reveals that periodically incoming radiation, interacting with the heat-sensitive VO_2 film, leads to the formation of a minor hysteresis loop. The phenomenon is not treated by classical hysteresis models, such as the integral Preisach[13] and the differential Jiles model,[14] which are both unsuited for hysteresis modeling in the present application.

Accurate device modeling, being essential to identify optimum operation requirements, thus relies on implementation of an appropriately adapted hysteresis model. As a function of operating and biasing conditions, and in the presence of strong electrothermal feedback, the following figures of merit were explored: characteristics of device output signal and responsivity, associated linear dynamic range, response times and frequency range of operation, bolometer noise, and achievable detectivities.

Finally, the present investigation includes an evaluation of the optical absorptivity ε and associated spectral range for the device under consideration, covering the wavelength range $0.35 < \lambda < 10$ μm.

2 Device Design and Modeling

In this work, a follow-up to earlier reported bolometer performance studies is presented. It refers to both a superconducting high-T_C transition-edge microbolometer[15] and a VO_2-based transition-edge device explored, however, in the absence of electrothermal feedback effects.[16] The design route under consideration comprises a very thin (50- to 100 nm) semitransparent and optically absorbing VO_2 film, deposited onto a square supporting Si membrane of size 1×10^{-2} cm^2 and thickness 1 μm. To maintain mechanical integrity of the device both G_{eff} and C_{eff} must be sufficiently high. Here, the supporting membrane is fully suspended and thermally coupled via a high coupling coefficient G_{eff} to the surrounding, massive Si substrate. It serves as a temperature-controlled heat spreader, mounted on a current-controlled Peltier element. Details of the associated thermal control loop are not further elaborated here. The thermophysical properties of the present device arrangement, defined by C_{eff} and G_{eff}, largely originate from the supporting Si membrane.

Temperature adjustment of the operation point within the transition can be achieved by means of a Peltier-element cooler thermoelectric (TEC). Since the transition region is above ambient T, the TEC will be operated at low bias in heating mode, and the Si substrate of the VO_2 sensor device attached to the TEC hot plate. Its cold site is connected to an air-blown heat sink, which exhibits a sufficiently large heat capacity. However, for high electrical device biasing under strong electrothermal feedback, thermoelectric cooling would be required to compensate Joule device heating. State-of-the art TECs provide sufficient cooling capacity. An appropriately designed TEC stabilization system has been reported in Ref. 17, where temperature stability of 2.5 mK has been established. For moderate values of the transition width (4 to 6 K), thermal stability of ±100 mK can be considered sufficient for bolometer operating points within the transition region. In connection with a high-heat-capacity heat sink, an appropriately designed proportional-integral (PI) control circuit for the TEC can be implemented that would fully suppress fast thermal fluctuations that appear in high-rate IR imaging applications.

2.1 *Electrothermal Response Model*

The heat balance equation appropriately describes the physical function of a bolometer. The numerical Simulink simulations included the thermal control loop, implemented with a proportional integral-derivative controller. Thus, easy-to-explore analytical expressions defining the figures of merit are not available for this work. The differential equation has been combined with a previously developed hysteresis model, precisely matched to the R-T characteristics of the VO_2 film.[7] The earlier-used thermal device parameters C_{eff} and G_{eff}, ascribed to a superconducting Si-membrane transition-edge device[3] have been adopted in the present bolometer design. Briefly, the heat balance equation is expressed as

$$C_{\mathrm{eff}} \frac{d(T_S - T_H)}{dt} = (J_{\mathrm{CCM}} \text{ or } J_{\mathrm{CVM}} \text{ or } J_{\mathrm{CTM}}) - G_{\mathrm{eff}}(T_S - T_H) + \varepsilon P_0, \qquad (1)$$

where εP_0 is the absorbed input radiation power, ε is the optical absorptivity, T_S is the sensor temperature, T_H is the heat-sink temperature, G_{eff} incorporates the coupling coefficient and thermal conductivity from the heat-sensing element to the heat sink, C_{eff} is the thermal energy stored at the device, and $J_{V,I}$ is the Joule power applied by electrical biasing of the device with current I_b or voltage V_b. It is given as $J_{\mathrm{CCM}} = I_b^2 R_S$ for CCM operation with voltage readout and negative electrothermal feedback, and as $J_{\mathrm{CVM}} = V_b^2/R_S$ for CVM operation, current readout, and positive electrothermal feedback. Under very low electrical bias values and absence of ETF, an inherent sensor-specific response time can be defined as $\tau_i = C_{\mathrm{eff}}/G_{\mathrm{eff}}$. As is evident from Figs. 2–6 in Sec. 3, the device temperature, biasing conditions, and input radiation levels crucially affect device performance and dynamic properties. Under equilibrium conditions, i.e., $\mathrm{d}(T_S - T_H)/\mathrm{d}t = 0$, in the absence of input radiation εP_0, the actual sensor temperature T_S is determined by G_{eff}, the applied Joule biasing power $J_{\mathrm{CCM,CVM}}$, and adjusted heat sink temperature T_H according to

$$T_S = \frac{J_{\mathrm{CCM,CVM}}}{G_{\mathrm{eff}}} + T_H. \tag{2}$$

2.2 *Electrical Biasing Conditions*

To avoid thermal instability under conditions of positive ETF, bias levels must not exceed a critical value V_b. According to Ref. 18 the critical voltage for simple negative temperature coefficient (NTC) thermistor materials like Ge can be written as $V_b^2 = -GR_0/\beta$. At higher bias voltages, thermal runaway usually occurs, along with device destruction. However, the simplified model does not apply for transitions-edge devices, where R_0 and β are not constant quantities, but vary strongly with temperature. V_b also is affected by the presence of minor-loop hysteresis, and decreases with increasing radiation magnitude. Simulation runs indicated the appearance of an instability at $V_b > 1.3$ V. The critical bias voltage thus has been limited to a 10%-lower value, to maintain operation under safe conditions. However, it is important to note that the simulations did not display destructive thermal runaway above the critical voltage, but a rapid increase in the signal noise figure, along with unpredictable responsivity variations. This somewhat unexpected effect of self-stabilization under positive ETF in transition-edge devices will be described elsewhere.[19] The bias current I_b under conditions of negative ETF has been arbitrarily limited to 2.1 mA, mainly to avoid excessive cooling of the heat sink far below ambient temperature.

2.3 VO_2 *Hysteresis Model*

Briefly, the purely algebraic so-called limiting loop (L^2P) hysteresis model comprises a set of four adjustable parameters to fully describe a hysteretic transition.[20] It includes the behavior of major, minor, and nested loops, as well as the loop accommodation process. This phenomenon is particularly important for accurate bolometer simulation. To reduce the processing time for the lengthy calculations, minor-loop accommodation was terminated after 10 cycles. The hysteretic variation of the VO_2 film resistance as a function of temperature, $R_S(T_S)$, can be expressed in an algebraic form as

$$R_S(T_S) = 17 \exp\left(\frac{2553}{T_S + 273}\right) g(T_S) + 140, \tag{3}$$

where

$$g(T_S) = \frac{1}{2} + \left(1 + \tanh \beta\left\{\delta\frac{w}{2} + T_C - \left[T_S + T_{\mathrm{pr}} P\left(\frac{T_S - T_C}{T_{\mathrm{pr}}}\right)\right]\right\}\right) \tag{4}$$

and

$$T_{\mathrm{pr}} = \delta\frac{w}{2} + T_C - \frac{1}{\beta}\,\mathrm{arctanh}(2g_r - 1) - T_r, \tag{5}$$

with

$$\delta = \mathrm{sign}\left(\frac{\mathrm{d}T_S}{\mathrm{d}t}\right) \tag{6}$$

denoting the sign function that defines the polarity of the rate of the temperature variation, applied to the film. The temperature T_{pr} is the proximity temperature at the start of a new branch, and $P(x)$ is the proximity function, with $x = (T_S - T_C)/T_{\mathrm{pr}}$, defined by

$$P(x) = \frac{1}{2}(1 - \sin \gamma x)[1 + \tanh(\pi^2 - 2\pi x)]. \tag{7}$$

2.4 *Noise Model*

The sensor noise is crucially affected by bias conditions, temperature, and operation frequency and determines the achievable sensor detectivity D^*. The crucial device figure of merit is defined as $D^*_{V,I} = F^{1/2} S_{V,I}/\langle \delta V^N_{\mathrm{tot}}, \delta I^N_{\mathrm{tot}}\rangle$. Noise modeling has been performed, adopting the same model with refined parameters that was reported earlier in detail in Ref. 21 for the superconducting high-T_C transition-edge microbolometer. Briefly, four individual contributions, $\langle \delta I_i^N\rangle$ and $\langle \delta V_i^N\rangle$, constitute the total device noise voltage $\langle \delta V^N_{\mathrm{tot}}\rangle = (\Sigma_{i=1}^4 \langle \delta V_i^N\rangle^2)^{1/2}$ in the CCM, as

$$\langle \delta V^N_{\mathrm{tot}}\rangle = \left(4k_B T_C R_C + \frac{S_V^2 8F\sigma k_B T_B^5}{\eta} + \frac{S_V^2 4k_B T_C^2 G_{\mathrm{eff}}}{\eta} + \frac{K_N I_B^2 R_C^2}{Adf^n}\right)^{1/2}, \tag{8}$$

and the total current noise $\langle \delta I^N_{\mathrm{tot}}\rangle = (\Sigma\langle \delta I_N^2\rangle)^{1/2}$ in the CVM is likewise

$$\langle \delta I^N_{\mathrm{tot}}\rangle = \left(\frac{4k_B T_C}{R_C} + \frac{S_I^2 8A\sigma_B k_B T_B^5}{\eta} + \frac{S_I^2 4k_B T_C^2 G_{\mathrm{eff}}}{\eta} + \frac{K_N V_B^2}{R_C^2 Adf^n}\right)^{1/2}. \tag{9}$$

The individual noise contributions are called, in order, the frequency-independent resistance (Johnson) noise; the background radiation (photon) noise; the thermal fluctuation (phonon) noise induced by thermal contact and exchange with the heat sink; and finally the frequency-varying (flicker) $1/f$ noise. Both photon and phonon noise scale with the frequency-dependent sensor responsivity.

Table 1 Film parameters and physical constants.

Quantity	Unit	Value
Boltzmann constant k_B	J/K	1.38×10^{-23}
Stefan-Boltzmann radiation constant σ_B	W/(cm^2 K^4)	5.67×10^{-12}
Background temperature T_B	K	300
Optical absorptivity ε		0.5
Film area A	cm^2	10^{-2}
Film thickness h	cm	10^{-5}
Frequency exponent n		1
Frequency f	s^{-1}	$10^{-1}<f<10^{6}$
$1/f$-noise scaling factor K_N	cm^3	3.2×10^{-18}
Thermal coupling coefficient G_{eff}	W/K	460×10^{-8}

To quantify the dominating $1/f$ noise contribution for VO_2 films, we here use the approach described earlier in Ref. 22. There are no experimental data available on the Hooge coefficient of VO_2 films, commonly required to quantify the $1/f$ noise contribution. Thus, the flicker noise expression has been replaced with an empirical formula, including an experimentally determined noise scaling factor K_N that varies over 4 orders of magnitude from 3.2×10^{-18} to 2.4×10^{-22}, similar to the noise-modeling approach from Ref. 23. This quantity crucially depends on the film quality, and scales with the grain size of the VO_2 film. The parameters entering into the noise model are listed in Table 1.

2.5 *Optical Model*

The optical absorptivity ε has been determined, using the Fresnel equation system in its matrix representation. Real and imaginary refractive index values for VO_2 and Si have been taken from Refs. 24 and 25. Calculations have been performed using optical constants at 300 and 350 K in the purely semiconducting and the SMT state of VO_2, respectively. The geometry corresponds to a bilayer system, comprising a thin VO_2-film at various thicknesses $0<d<100$ nm, on a 1-μm-thick supporting Si membrane. Calculations were performed at perpendicular radiation incidence, covering the wavelength range $0.35<\lambda<10\ \mu$m.

3 Results and Discussion

Figure 1(a) displays the calculated R-T hysteresis curve, matched to the experimentally recorded thermal resistance variation of a thin VO_2 film sputter-deposited onto a Si substrate. The inset shows a pulse train of applied rectangular radiation, and illustrates the related temporal voltage response of the film in the CCM. Associated minor-loop formation and accommodation pertaining to the pulse train are resolved within the descending major loop. Figures 1(a)–1(c) outline the associated variation of the electrical

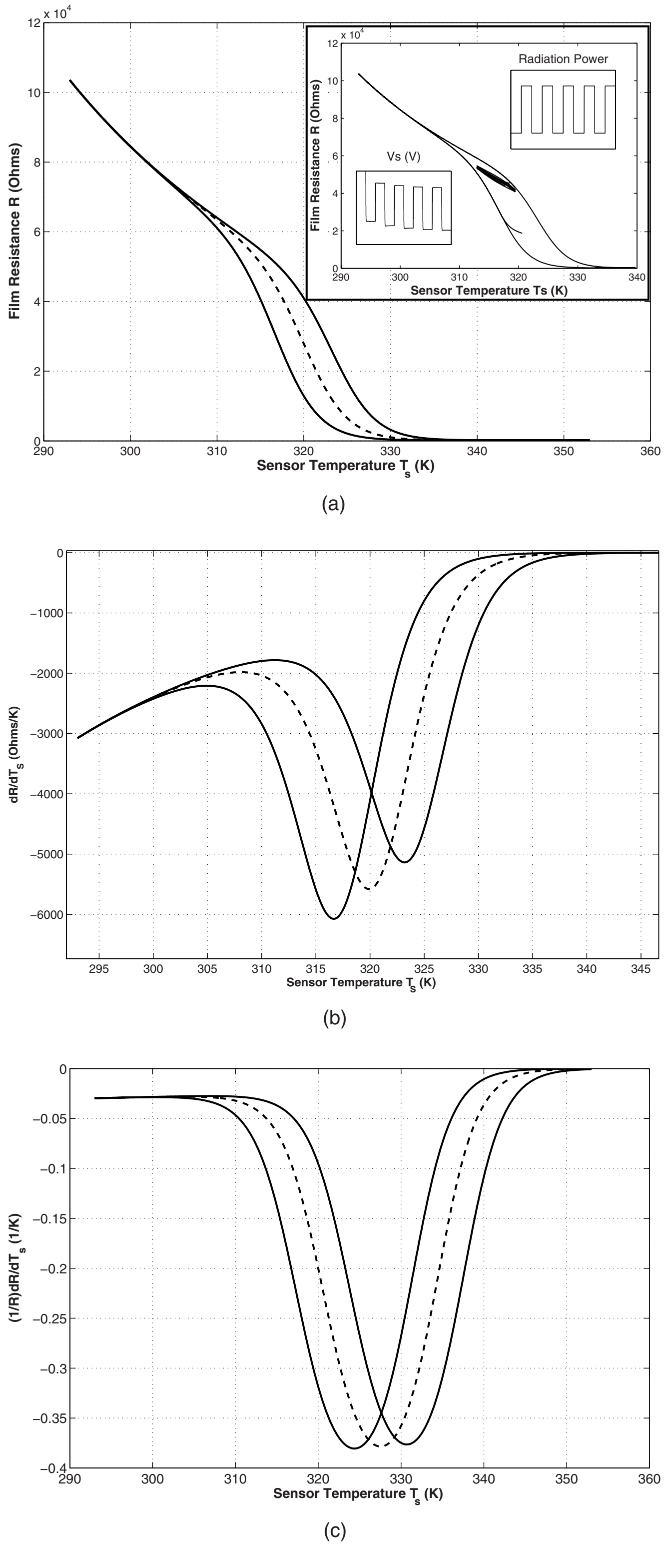

Fig. 1 (a) Variation of VO_2-film resistance as function of T_S within the phase transition. Hysteresis width is set at 6.5 K, total transition width approximately 35 K. The broken line indicates the hysteresis-free limit. Inset illustrates minor-loop formation in the descending branch. Upper right pulse train resembles the thermal input signal; lower left inset shows the voltage response signal due to minor-loop formation. (b) dR_S/dT_S as function of T_S for the descending, ascending, and central branches. (c) The associated $\beta=(1/R_S)\,dR_S/dT_S$ as function of T_S.

VO_2 film parameters dR_S/dT_S and $\beta=(1/R_S)dR_S/dT_S$. The hysteresis width was set to 6.5 K. Pronounced, separated minima are resolved for both dR_S/dT_S and negative values of the TCR, connected to the ascending and descending $R_S(T_S)$ curves. The TCR is −3% in the semiconducting phase, but increases to −38% within the transition region. The central broken line indicates the SMT in the absence of hysteresis. Note that the minima from dR_S/dT_S and $(1/R_S)dR_S/dT_S$ are displaced by approximately 9 K.

Figures 2(a) and 2(b) outline the influence of ETF via electrical device biasing on operation conditions. Data were obtained at an input radiation level of 1 mW, revealing opposite variations of the response time τ. In the CVM, τ increases weakly from 0.5 to 0.63 ms with increasing bias voltage. In contrast, in the CCM, an almost linear decrease of the response time appears with increasing bias currents. At $I_b=2$ mA, τ decreases from 0.5 ms to 145 μs. In the CVM, the critical bias voltage is limited to $V_b<1.17$ V. At higher bias values sensor instability is imminent, but is absent for negative ETF conditions of the CCM. The inset to Fig. 2(a) reveals the influence of the accommodation process, which requires >30 cycles for stabilization, revealing a stronger effect in the CVM. Figure 2(b) displays the variation of the heat-sink temperature T_H as a function of bias. In both operation modes, T_H needs to be adjusted below ambient temperature by increasing the bias voltage or current, to secure optimum operation at T_S, in accordance with Eq. (2). The ETF effect is much more pronounced in the CCM. The inset to Fig. 2(b) illustrates the linear relation between sensor temperature T_S and heat-sink temperature T_H at low bias current or voltage. Thermoelectric (Peltier) cooling devices, conveniently used to maintain T_H, are appropriate for bias currents ≤ 2 mA.

Figures 3(a)–3(d) illustrate the influence of the radiation input on the device output signal and the related response times. Both device features reveal complex, largely nonlinear variations with the input signal. Figures 3(a) and 3(b) display the characteristics under CCM operation for different current biases. At low radiation levels, the voltage response scales approximately linearly. At higher radiation levels, a shift is observed and smaller slope, until signal saturation appears, attributed to the control circuit. The curve slope and ratio of the respective output signals with radiation power provides the device responsivities $S_{V,I}=d(V_S,I_S)/dP$, representing crucial figures of merit. The linear dynamic range extends up to 8 mW at high bias current. For low bias and radiation magnitudes, the response time varies weakly, decreases with increasing bias current at low radiation levels, but displays a pronounced maximum at higher radiation input.

The displayed device characteristic is substantially different for CVM operation. Here, the current response throughout increases nonlinearly with the radiation level and bias voltage, resulting in a very small linear dynamic range, $\ll 1$ mW at high bias, but increasing at low applied voltage to about 3 mW. For very low radiation levels, τ shows little variation with radiation power and voltage bias. The dynamic response changes drastically with higher bias and radiation input, leading to a sharp maximum around 4 mW, along with decreasing response times at higher input signals.

Figures2 4(a)–4(d) illustrate the effects of operation and biasing conditions on the device responsivities $S_{V,I}$. Figure 4(a) outlines the variation with temperature for both operation modes, using logarithmic scaling. Bolometric response data, obtained at 1-mW radiation input, were calculated from the descending $R_S(T_S)$ curves. Distinct differences between the two modes are resolved, including separated maxima at 320.5 K for the CCM with 380 V/W, and at 334.41 K for the CVM with 0.15 A/W. The former extended feature approximately follows the inverted dR_S/dT_S curve from Fig. 1(b). It steadily increases toward lower temperature, well into the semiconducting phase. The CVM response characteristics—at substantially lower magnitude—roughly resembles the inverted temperature variation $\beta(T_S)$ of the TCR from Fig. 1(c). The bell-shaped, sharply localized feature is shifted by 14 K to higher T_S.

The inset to Fig. 4(b) illustrates the action of the minor-loop accommodation process, being similar to the inset to Fig. 2(a). The associated nonlinear variation of $S_{V,I}$ with biasing conditions is shown in Fig. 4(b). An extended, broad maximum around 1.5-mA bias current is resolved in the CCM. In the CVM, S_V increases steadily with bias voltage, but is limited to 1.17 V to avoid operational instability. Figure 4(c) shows the Bode plots $S_{V,I}(f)$ within the range $10^{-1}<f<10^4$ Hz. Data were taken at low bias current or voltage, in the absence of ETF effects, where the 3-dB rolloff appears at about 600 Hz for both modes. With higher bias currents, it would shift to higher values, due to the reduction of the time constant, in accord with the findings of Fig. 2(a). Figure 4(d) shows the variation of $S_{V,I}$ with hysteresis width w, taken as a structural-material quality parameter. The data indicate a substantial device improvement of approximately a factor 4 in the absence of hysteresis of the SMT, while little variation in the responsivity has been found for hysteretic transitions within the range $2<w<10$ °C.

Figures 5(a)–5(d) illustrate the effects of operation and biasing conditions on the current and voltage noise magnitudes $\langle \delta I_{\mathrm{tot}}^N \rangle$ and $\langle \delta V_{\mathrm{tot}}^N \rangle$, with 1-Hz bandwidth. Figure 5(a) outlines the variation with temperature, using logarithmic scaling to include both quantities. Both noise figures appear inverted, displaying mirror symmetry around the T_S axis, and the output voltage fluctuations in the CCM substantially exceed the noise magnitude $\langle \delta I_{\mathrm{tot}}^N \rangle$ of the CVM. The variation of the noise figures with the biases is shown in Fig. 5(b). In both modes, a nonlinear increase with bias current and voltage is seen. Again, the bias voltage in the CVM is limited to 1.17 V to avoid device instability. Figure 5(c) shows the variation of both noise figures with frequency within the range $10^{-1}<f<10^4$ Hz with log-log scaling. Both noise figures decline at an identical rate $\approx f^{-1/2}$ indicating a dominating flicker noise contribution. Figure 5(d) shows the corresponding variation of $\langle \delta I \rangle$ and $\langle \delta V \rangle$ with the hysteresis width w, taken as a structural-material quality parameter. The data indicate a minor decrease for the CVM towards an anhysteretic characteristic of the SMT, while no variation of the noise figures is resolved within the range $2<w<10$ °C.

The noise figures $\langle \delta V_{\mathrm{tot}}^N \rangle$, within the frequency range $1<f<1000$ Hz of a current-biased VO_2 film at the center

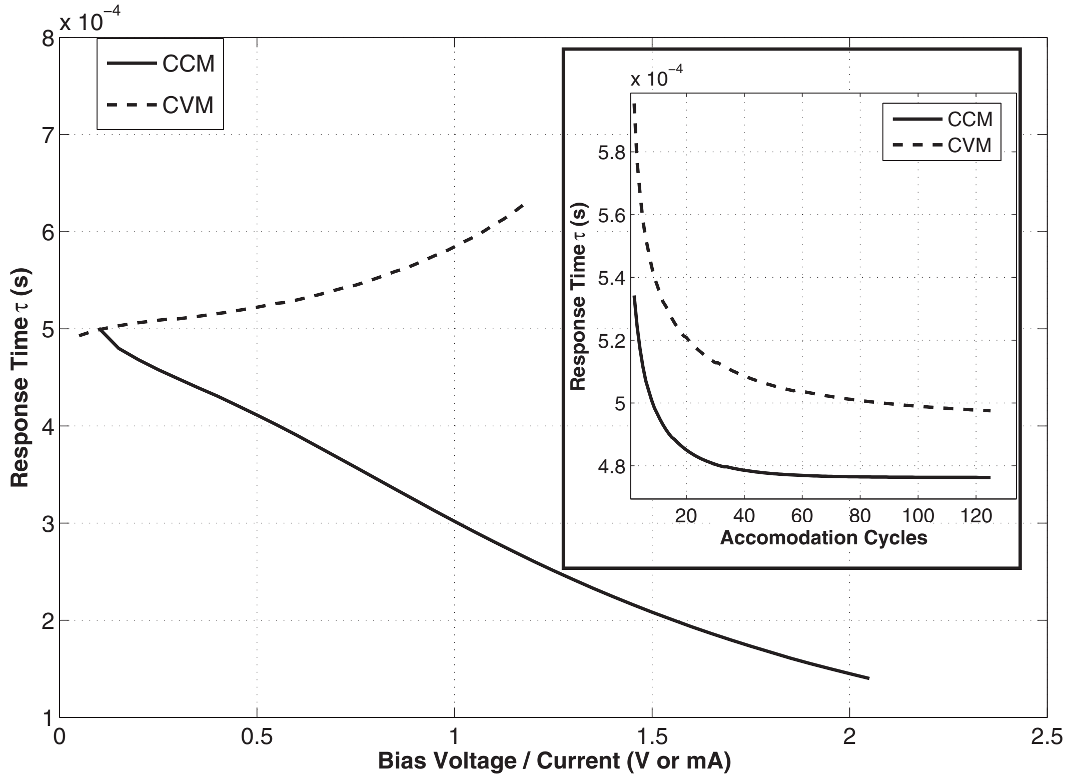

(a)

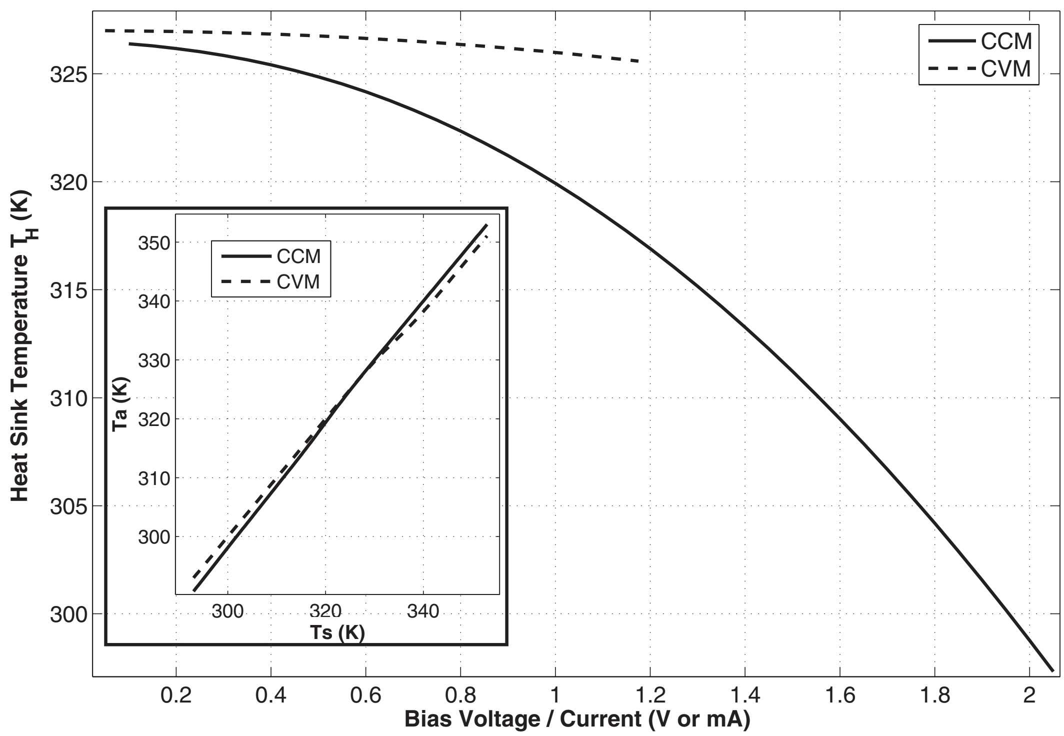

(b)

Fig. 2 Variations of (a) response time τ and (b) heat-sink temperature T_H with biases I_b and V_b. The broken line indicates CVM, the solid line CCM operation. Inset to (a) indicates the effect of loop accommodation and stabilization. Inset to (b) illustrates the nearly linear variation of heat-sink temperature T_H with sensor temperature T_S, recorded at low bias.

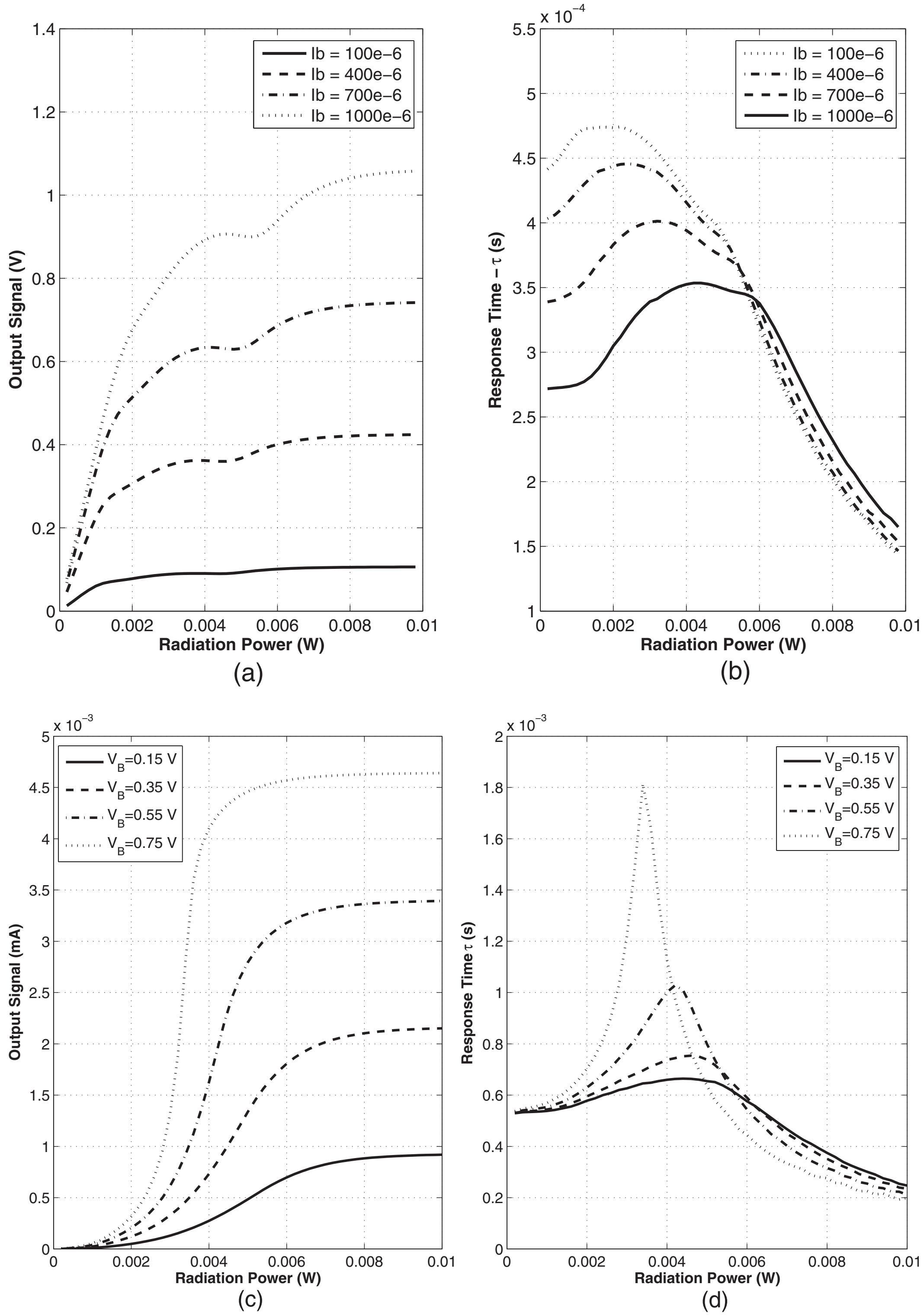

Fig. 3 Variation of device output signals [(a) to (c)] and response times [(b) to (d)], displayed as functions of the input radiation magnitude, under different biasing conditions. The associated slopes dV_S/dP and dI_S/dP provide the responsivity in the CCM and CVM.

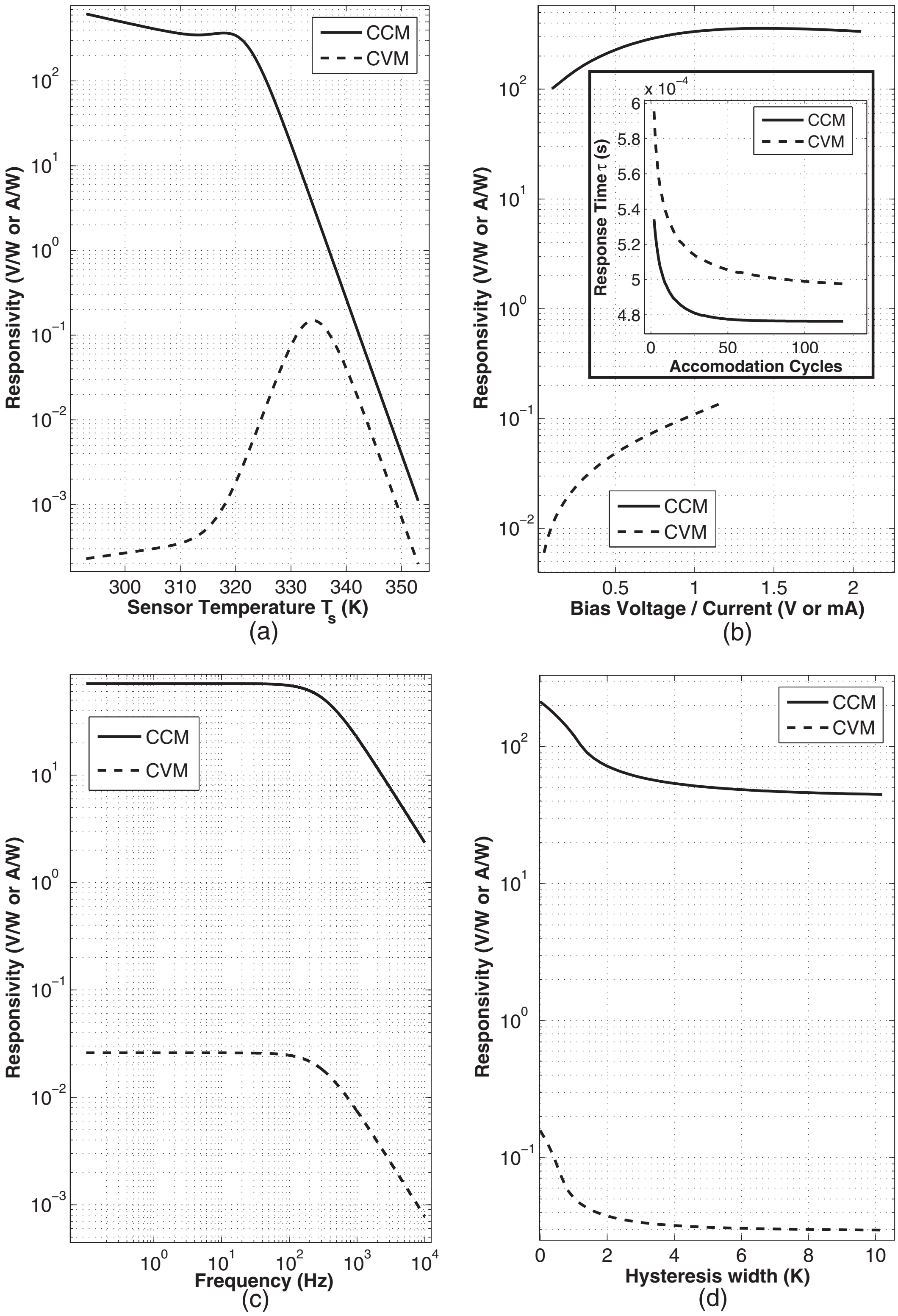

Fig. 4 Variation of device responsivities for CCM and CVM, displayed as functions of (a) T_S, (b) electrical biases, (c) frequency, and (d) hysteresis width, shown in log scaling. Inset to (b) outlines the influence of the loop accommodation process on sensor responsivity.

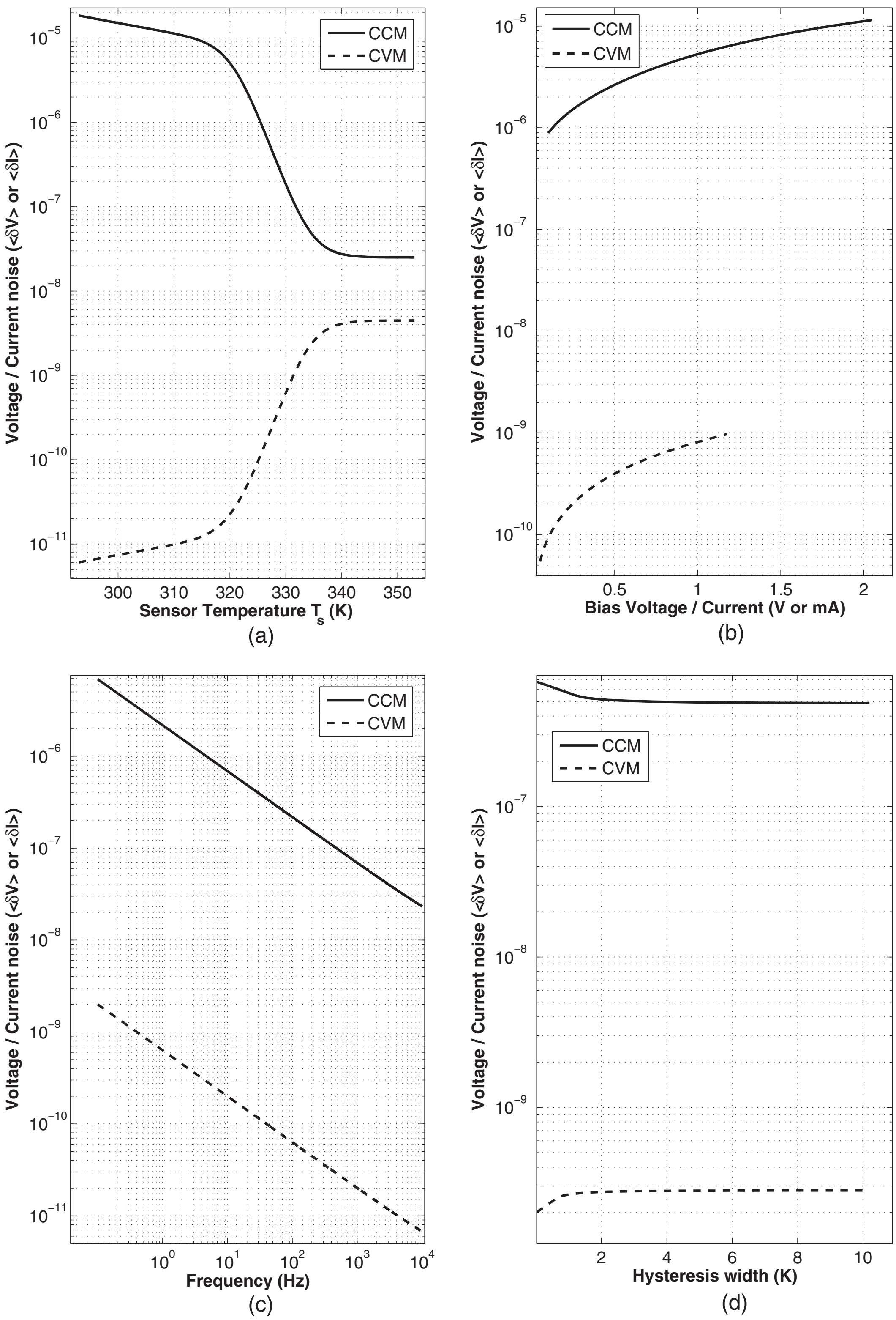

Fig. 5 Variations of the total current and voltage noise magnitudes for CCM and CVM, displayed as functions of (a) sensor temperature T_S, (b) electrical biases, (c) frequency, and (d) hysteresis width, shown in log scaling.

of the transition at 50 °C and in the semiconducting state at 18 °C can be seen in Fig. 4 of Ref. 16, indicating dominance of $1/f$ noise in the material. Generally, recorded voltage noise magnitudes are substantially higher in the semiconducting state, in accord with the results of the present noise model. The change of slope of $\langle \delta V_{tot}^N \rangle$ at $f < 30$ Hz (see Fig. 4 of Ref. 16) in the transition region (50 °C) indicates the presence of a second, yet unidentified noise mechanism, not considered in the present work. A detailed noise analysis of VO_2 films has been reported previously in Ref. 26.

Figures 6(a)–6(d) illustrate the effects of operation and biasing conditions on the device detectivity $D_{V,I}^*$, earlier chosen as a quantitative parameter of device performance. The variation with sensor temperature T_S in Fig. 8(a) shows pronounced maxima, located in both modes at 328 K. Thus, the previously reported peak separation of 14 K in Fig. 4(a) for the respective device responsivities is lifted for $D_{V,I}^*$. While the performance in the CVM is superior to that in the CCM within the transition region, the advantage disappears for operation in the semiconducting phase, where device detectivities are almost identical, and substantially lower for both modes. The effect of the biases I_b and V_b on the device performance is shown in Fig. 6(b). A steady degradation appears in the CCM with increasing bias current, similar to the result of Fig. 2(a), but is absent in the CVM. At low bias, in the absence of ETF, identical detectivities were found. The influence of operating frequency is shown in Fig. 6(c), where pronounced maxima at 300 Hz are resolved. The rapid device degradation towards lower frequency is due to the detrimental, large contribution of $1/f$ flicker noise, while the decrease in detectivity with increasing f is attributed to the degrading responsivity curve at high frequency, as seen in Fig. 4(c). Figure 6(d) illustrates the D^* variation with hysteresis width, where towards anhysteretic conditions a pronounced improvement of almost one order of magnitude is observable for CVM operation. The inset to Fig. 6(b) shows the ratio D^*/τ for operation in both modes as a function of bias. Due to the decreasing response time in the CCM, as displayed in Fig. 2(a), the associated D^* values remain balanced, leaving almost identical overall device performance for the two modes.

The strong influence of the earlier-mentioned flicker noise on the device performance is shown in Fig. 7, where D^* is plotted as a function of the associated prefactor K_N. The analysis reveals that a substantial improvement of D^* of up to 7×10^8 cm Hz$^{1/2}$ W^{-1} is achievable in the CVM. The associated relation between film quality and K_N is illustrated in the inset to Fig. 7, where experimental findings from Table 1 of Ref. 22 are plotted in logarithmic scaling. A remarkable, sharp increase of K_N and related degradation of device performance is observable with increasing phase transition width of the VO_2-film material. No clear correlation has been identified between hysteresis width and K_N.

Finally, Figs. 8(a) and 8(b) illustrate the spectral detection range of the microbolometer for both the center of the SMT at 355 K and the semiconducting state at 300 K, displayed in the inset. The device absorptivity ε has been obtained at perpendicular radiation incidence. Two cases have been evaluated: placement of the VO_2 film below the Si membrane [Fig. 8(a)] and above the Si membrane [Fig. 8(b)]. In the former case strong oscillatory behavior is found, while in the latter one sees a smooth absorptivity decrease towards longer wavelength. The optical quantity ultimately scales with D^*, covering the wavelength range $0.35 < \lambda < 10$ μm, and displays pronounced spectral variations. The absorbed radiation transforms into heat, thus changing the film resistance, with the two device materials contributing differently. Since silicon is optically transmitting below its optical band gap, (photon energies < 1.05 eV), the thin membrane support accounts for high ε and D^* values within the visible to near-infrared (NIR) wavelength region, at $0.35 < \lambda < 1$ μm. The optical absorption feature extending into the far infrared (FIR) region; thus is attributed primarily to the optical properties of the VO_2 film, being remarkably different in the SMT and the semiconducting phase. The spectral absorption range has been examined here for $\varepsilon \approx 0.2$ at 100-nm VO_2-film thickness. Within the SMT, the spectral range extends into the FIR region up to $\lambda = 6$ μm, but is limited to < 1.3 μm in the semiconducting phase at 300 K, as illustrated in the inset.

The present device evaluation for a NTC material clearly demonstrates the inverted sensing characteristic of VO_2 films, compared to the earlier-mentioned high-T_C superconducting transition-edge devices, exhibiting positive TCRs. This is immediate from Fig. 1(b) of Ref. 15, where a localized, bell-shaped response curve appears in the CCM with positive ETF, but a substantially extended operation range toward decreasing T_S appears in the CVM, due to negative ETF. Similarly, the sensor dynamics is strongly affected by biasing: with achievable response time $\tau < 10$ μs for the high-T_C transition-edge device under high bias voltages in the CVM from Fig. 1(b) of Ref. 15, the superconducting device provides a much shorter response time than the VO_2 microbolometer. According to Fig. 2(a), at high bias currents of 2 mA, the shortest achievable τ under strong ETF decreases to 145 μs. Evidently, the inverted sensor characteristic results from the opposite signs in the TCR for the different materials, which alternate the action of positive versus negative electrothermal feedback.

Substantial differences also appear in the magnitude of achievable device detectivity: experimental high-T_C superconducting transition-edge devices have been reported with D^* values as high as 1.6×10^{10} cm Hz$^{1/2}$ W^{-1} under positive ETF and at low operation frequency in Ref. 4. For low-T_C devices, D^* even may increase up to 10^{18} cm Hz$^{1/2}$ W^{-1}. In contrast, as visible from Fig. 7, attainable D^* values for VO_2 in the present design, at moderate noise magnitudes, would remain $< 1 \times 10^8$ cm Hz$^{1/2}$ W^{-1}. This quantity remains well within the limits known for other noncooled thermal detectors, including high-T_C microbolometers based on yttrium barium copper oxide, operated far from the phase transition.[27] The reduced performance of the VO_2-microbolometer compared to the superconducting devices primarily originates from the much higher operating temperature (330 versus 90 K), which leads to substantially higher resistance (Johnson) and phonon noise contributions, scaling with T_C and T_C^2, respectively. Experimental bolometer matrices reported in Ref. 22 compare well with the present analysis, with $D^* \approx 5 \times 10^7$ cm Hz$^{1/2}$ W^{-1} for $K_N = 4.4 \times 10^{-20}$ cm^{-3}, obtained in the CCM.

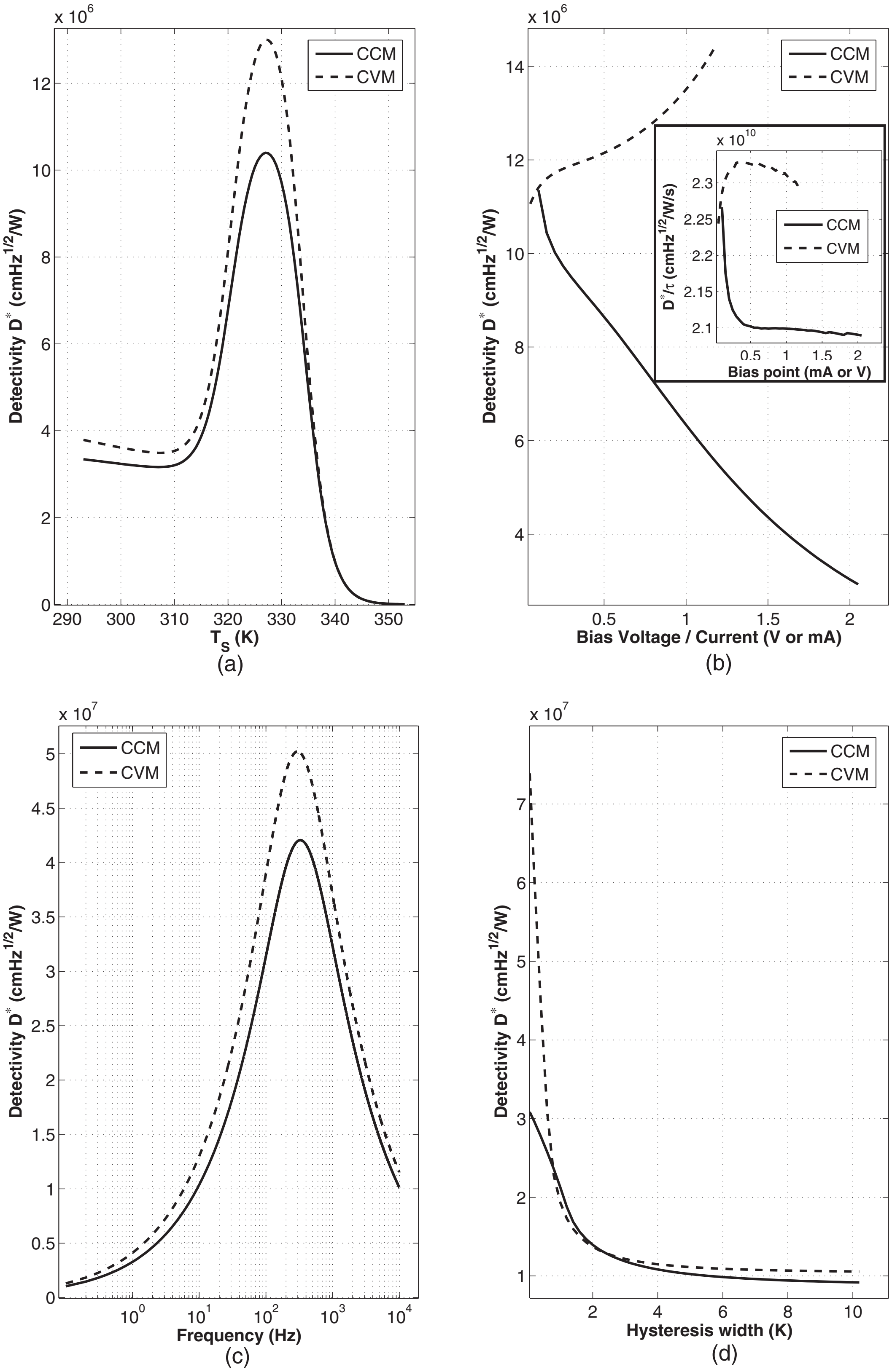

Fig. 6 Variations of device detectivities D^* for CCM and CVM, displayed as functions of (a) T_S, (b) electrical biases, (c) frequency, and (d) hysteresis width, shown in log scaling. Inset to (b) illustrates the overall detectivity D^*/τ as a function of electrical biases.

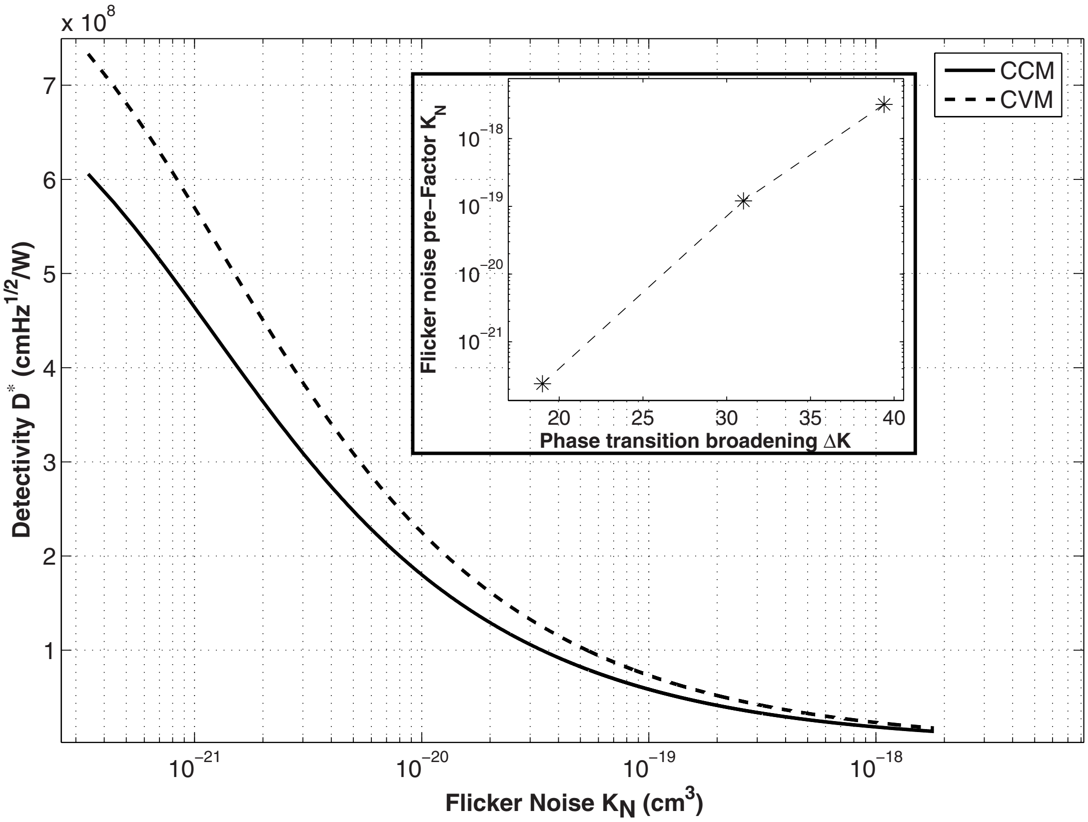

Fig. 7 Variations of device detectivity D^* for CCM and CVM, displayed as a function of flicker noise prefactor K_N. Inset illustrates the experimentally determined variation of K_N with the phase transition broadening.

Experimental 32×32 two-leg-suspended microbolometer arrays have been reported in Ref. 28, employing nonstoichiometric VO_2 films. The devices were operated in the CVM, in the absence of a clear SMT phase transition, attaining moderate $D^*\approx 2.1\times10^8$ cm $Hz^{1/2}$ W^{-1} at τ=10 ms, using blackbody (8- to 12-μm wavelength) input radiation. Figure 6 of Ref. 28 confirms the simulation results of Fig. 6(b) of this work, where an increase of D_V^* with the bias voltage is predicted for CVM operation. Micromachined bolometer devices reported in Ref. 5, with a similar design and in the absence of an SMT, yielded somewhat lower performance, $D^*\approx 1.1\times10^7$ cm $Hz^{1/2}$ W^{-1}, at low bias currents, with τ=0.723 ms. An alloyed vanadium-tungsten oxide film served as the sensing material, deposited onto Si_xN_y membranes. Electrical recordings were taken in the CCM, using optical input by the FIR radiation of a CO_2 laser at 10.6-μm wavelength. To maintain optical absorption in the FIR region, an additional NiCr film was used in the design. ETF effects were not considered in the device evaluations.

As illustrated before, the performance of VO_2 microbolometer devices can be substantially improved by optimal selection of electrical biasing conditions and selected mode of operation, sensor and heat-sink temperature, frequency range, and the VO_2 film material with regard to optical and noise properties. Virtually all results indicate CVM superior to CCM operation; an increase of 30% in D^* is seen in Fig. 6(a). This figure also illustrates that high performance in either mode requires setting T_S=326 to 328 K. Comparison with Fig. 4(a) shows that the best operation temperature for optimum D^* does not exactly agree with T_S for the highest responsivity. Therefore, achievement of the optimum T_S would require control of T_H, most easily achieved with thermoelectric cooling devices.

An important requirement, particularly for the signal readout circuitry, is the increase of D_V^* with bias voltage in the CVM [Fig. 6(b)], which would allow use of the full instrumental dynamic range without performance degradation. Since the CCM displays the opposite characteristic, high D_I^* values for current-biased sensors are only established at low bias, thus limiting the dynamic range. The frequency characteristics of dominating flicker noise crucially affect the variation of D^* with frequency [Fig. 6(c)]. The large noise contribution at low f in both modes displaces the maximum of D^* towards high frequencies. Therefore, reticulation at around 300 Hz in both modes would be required to establish optimum performance. Reducing the $1/f$ noise contribution thus is an efficient approach to improve device performance at frequencies compatible with video frame rates. As outlined before, recent improvements of VO_2 film deposition methods are suited to substantially reduce flicker noise contributions. A phase transition broadening ΔT_B of around 25 °C has been achieved recently[29] for annealed polycrystalline VO_2 films, rf-reactively sputtered onto float glass. In Ref. 1, a ΔT_B value as low as 15 °C for single-crystalline, pulsed-laser-

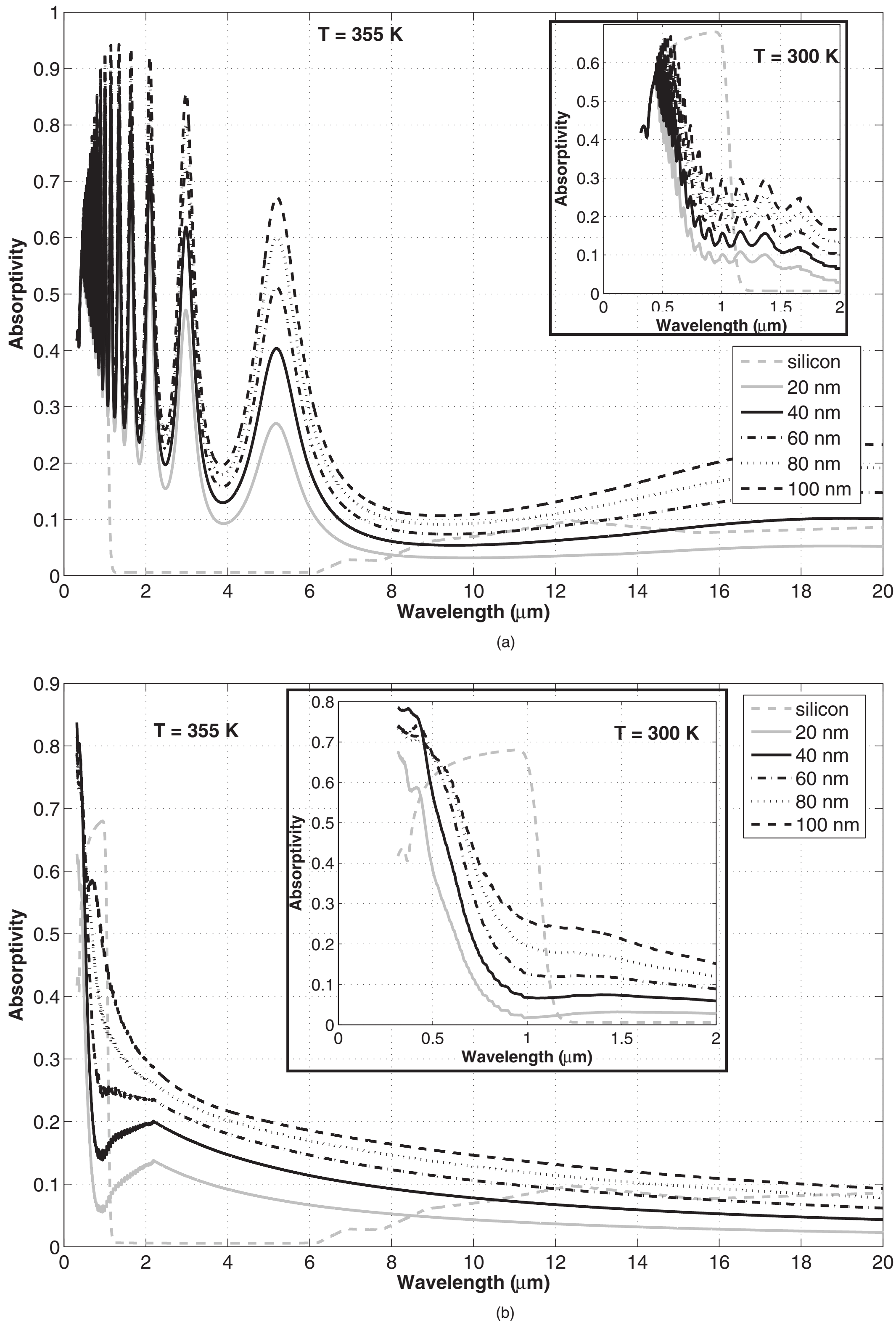

Fig. 8 Variation of the optical device absorptivity ε at 355 K within the SMT, displayed as a function of wavelength: (a) air-Si−VO_2 configuration; (b) air-VO_2−Si configuration. Data were obtained at perpendicular incidence D^*, calculated for a range of VO_2 film thickness $0<h<100$ nm. Inset displays ε for 300 K in the semiconducting state.

deposited (LPD) films on sapphire {0001} substrates has been reported. In view of the K_N-ΔT_B relationship shown in the inset of Fig. 7, flicker noise prefactors of 5×10^{-21} and 6×10^{-23} thus are achievable with optimized film deposition methods, which would lead to D^* values of 3×10^8 cm $Hz^{1/2}$ W^{-1} for polycrystalline and up to 1×10^9 cm $Hz^{1/2}$ W^{-1} for epitaxial VO_2 films.

The calculated optical absorptivity ε of Fig. 8 is in agreement with recent experimental findings of Ref. 29, where optical transmission data on VO_2 in the semiconducting and the SMT region were reported. Reduced spectral transmission and associated higher absorptivity have been observed in the SMT at 70 °C, covering the wavelength regime $\lambda<2.5$ μm. Although ε extends considerably into the FIR region ⟨10 μm⟩, its magnitude (≤ 0.2) remains rather low. Hence, to establish improved performance and detectivity, extending into the FIR region at wavelength $\gg 10$ μm, use of a highly absorbing, spectrally broadband absorber film, additionally deposited onto the heat-sensing VO_2, is essential. Here, use of efficient metallic absorber films, like gold black and ultrarough silver (silver black), would be beneficial. These specially prepared materials exhibit very high absorptivity, which extends well into the long-wavelength (terahertz) regime up to 100 μm, and offer good adhesion to Si substrates.[30]

In conclusion, the optical performance and crucial figures of merit of a hysteretic VO_2-based transition-edge microbolometer have been evaluated for constant current (CCM) and constant voltage (CVM) modes of operation. The analysis reveals an approximately factor-3 improved D^* value at the SMT, compared to the semiconducting regime. This ultimately suggests temperature-controlled device operation, with the use of a well-designed heat sink. Neither phase-transition hysteresis nor minor-loop accommodation deteriorates device operation. Strong electrothermal feedback leads to a highly nonlinear detector characteristic, along with pronounced differences between the two modes. The CVM consistently yields higher D^* values than the CCM, at the cost of a reduced linear dynamic range with regard to the incoming radiation level, which is substantially larger in the CCM. This mode exhibits a shorter response time at high bias current, at the cost of a pronounced degradation of the associated D^*. Both high detectivity at high bias voltage and limitation to low radiation levels suggest use of the CVM for imaging applications. The CCM would be beneficial for measurements at high radiation magnitudes, in connection with short response times or high-frequency operation, as in laser-beam profiling and characterization, or Fourier transform infrared (FTIR) spectroscopy.

For epitaxial, high-quality VO_2 films on sapphire substrates, very low flicker noise levels can be established, so that achievable D^* values approach those of superconducting high-T_C transition-edge devices operated around 90 K. Achievable response times of VO_2-based transition-edge devices under conditions of strong negative ETF (CCM) substantially exceed those of superconducting detectors and exclude their use as fast microcalorimeters for x-ray detection.

Acknowledgments

The authors would like to thank CNPq, FAPESQ, and CAPES for a research grant, financial support, and a study fellowship, respectively.

References

1. J. Narayan and V. M. Bhosle, "Phase transition and critical issues in structure-property correlations of vanadium oxide," *J. Appl. Phys.* **100**, 103524 (2006).
2. K. D. Irwin, G. C. Hilton, D. A. Wollman, and J. M. Martinis, "Thermal-response time of superconducting transition-edge microcalorimeters," *J. Appl. Phys.* **83**, 3978–3985 (1998).
3. H. Neff, J. Laukemper, I. A. Khrebtov, A. D. Tkachenko, E. Steinbeiss, W. Michalke, M. Burnus, T. Heidenblut, G. Hefle, and B. Schwierzi, "Sensitive high T_C transition edge bolometer on micromachined silicon membrane," *Appl. Phys. Lett.* **66**, 2421–2423 (1995).
4. M. J. M. E de Nivelle, M. P. Bruijn, R. De Vries, J. J. Wijnbergen, P. A. J. de Korte, S. Sanchez, M. Elwenspoek, T. Heidenblut, B. Schwierzi, W. Michalke, and E. Steinbeiss, "High-T_C bolometer for far-infrared detection" *J. Appl. Phys.* **82**, 4719–4726 (1997).
5. N. Chi-Anh, H.-J. Shin, K. T. Kim, Y.-H. Han, and S. Moon, "Characterization of uncooled bolometer with vanadium tungsten oxide infrared active layer," *Sens. Actuators, A* **123–124**, 87–91 (2005).
6. S. Chen, H. Ma, S. Xiang, and X. Yi, "Fabrication and performance of microbolometer arrays based on nanostructured vanadium oxide thin films," *Smart Mater. Struct.* **16**, 696–700 (2007).
7. L. A. L. de Almeida, G. S. Deep, A. M. N. Lima, and H. Neff, "Modeling of the hysteretic metal-insulator transition in a vanadium dioxide infrared detector," *Opt. Eng.* **41**, 2582–2588 (2002).
8. F. J. Morin, "Oxides which show a metal-to-insulator transition at the Néel temperature," *Phys. Rev. Lett.* **3**, 34– (1959).
9. A. Zylbersztejn and N. F. Mott, "Metal-insulator transition in vanadium dioxide," *Phys. Rev. B* **11**, 4383 (1975).
10. A. A. Velichko, G. B. Stefanovich, A. L. Pergament, and P. P. Boriskov, "Deterministic noise in vanadium dioxide based structures," *Tech. Phys. Lett.* **29**, 435 (2003).
11. H. Jerominek, F. Picard, and D. Vincent, "Vanadium oxide films for optical switching and detection," *Opt. Eng.* **32**(9), 2092–2099 (1993); C. D. Reintsema, E. N. Grossman, and J. A. Koch, "Improved VO_2 microbolometers for infrared imaging: operation on the semiconducting-metallic phase transition with negative electrothermal feedback," *Proc. SPIE* **3698**, 190–200 (1999).
12. J. Y. Suh, R. Lopèz, L. C. Feldman, and R. F. Haglund, "Semiconductor to metal phase transition in the nucleation and growth of VO_2 nano-particles and thin films," *J. Appl. Phys.* **96**, 1209 (2004).
13. F. Preisach, "Uber die magnetische Nachwirkung," *Physik* **94**, 277–302 (1935).
14. D. C. Jiles and D. L. Atherton, "Theory of ferromagnetic hysteresis," *J. Magn. Magn. Mater.* **61**, 48–60 (1986).
15. H. Neff, A. M. N. Lima, G. S. Deep, R. C. S. Freire, and E. Melcher, "Nonlinearity and electrothermal feedback of high T_C transition edge bolometers," *Appl. Phys. Lett.* **76**, 640 (2000).
16. L. A. L. de Almeida, G. S. Deep, A. M. N. Lima, I. A. Khrebtov, V. G. Malyarov, and H. Neff, "Modeling and performance of vanadium oxide transition edge microbolometers," *Appl. Phys. Lett.* **85**, 3605 (2004).
17. A. B. Kozlov, Y. V. Kulikov, V. G. Malyarov, and I. A. Khrebtov, "Temperature-stabilization system for an uncooled microbolometer array," *J. Opt. Technol.* **68**(1), 57–59 (2001).
18. G. B. Brandão, L. A. L. de Almeida, G. S. Deep, A. M. N. Lima, and H. Neff, "Stability conditions, nonlinear dynamics, and thermal runaway in microbolometers," *J. Appl. Phys.* **90**(4), 1999–2008 (2001).
19. L. A. L. de Almeida, G. Neto, and H. Neff, "Evidence of self-stabilization in transition edge devices operated under positive electro-thermal feedback," (in press).
20. L. A. L. de Almeida, G. S. Deep, A. M. N. Lima, and H. Neff, "Limiting loop proximity hysteresis model," *IEEE Trans. Magn.* **39**(1), 523–528 (2003).
21. H. Neff, I. A. Khrebtov, A. D. Tkachenko, E. Steinbeiss, W. Michalke, O. K. Semchinova, T. Heideblut, and J. Laukemper, "Noise, bolometric performance and aging of thin superconducting films on silicon membranes," *Thin Solid Films* **324**, 230–238 (1998).
22. V. Yu. Zerov, Yu. V. Kulikov, V. G. Malyarov, I. A. Khrebtov, I. I. Shaganov, and E. F. Shadrin, "Vanadium oxide films with improved characteristics for IR microbolometric matrices," *Tech. Phys. Lett.* **27**, 378–380 (2001).
23. N. Chi-Anh and S. Moon, "Excess noise in vanadium-tungsten oxide bolometric material," *Infrared Phys. Technol.* **50**, 38–41 (2007).
24. H. W. Verleur, A. S. Barker, Jr., and C. N. Berglund, "Optical properties of VO_2 between 0.25 and 5 eV," *Phys. Rev.* **172**, 788–798 (1968).

25. Virginia Semiconductor, Inc., "Optical properties of silicon," data sheet, http://www.virginiasemi.com/vsitl.cfm.
26. V. Y. Zerov, Y. V. Kulikov, V. N. Leonov, V. G. Malyarov, I. A. Khrebtov, and I. I. Shaganov, "Features of the operation of a bolometer based on a vanadium dioxide film in a temperature interval that includes a phase transition," *J. Opt. Technol.* **66**(5), 387–390 (1999).
27. H. Neff, J. Laukemper, G. Hefle, M. Burnus, T. Heidenblut, W. Michalke, and E. Steinbeiss, "Extended function of a high T_C transition edge bolometer on a micromachined Si membrane," *Appl. Phys. Lett.* **67**(13), 1917–1919 (1995).
28. H. Wang, X. Yi, J. Lai, and Y. Li, "Fabricating microbolometer array on unplanar read-out integrated circuit," *Int. J. Infrared Millim. Waves* **26**, 751–762 (2005).
29. G. Fu, A. Polity, N. Volbers, and B. Meyer, "Annealing effects on VO_2 thin films deposited by reactive sputtering," *Thin Solid Films* **515**, 2519–2522 (2006).
30. H. Neff, S. Henkel, J. K. Sass, E. Steinbeiss, P. Ratz, J. Mueller, and W. Michalke, "Optical properties of ultrarough silver films on silicon," *J. Appl. Phys.* **80**(2), 1058–1062 (1996), and references cited therein.

Biographies and photographs of authors not available.